An assessment of the role of soft electron precipitation in global ion upwelling

Robert J Redmon[1], W. K. Peterson[2], Laila Andersson[2],

Philip G Richards[3], and A.W. Yau[4]

[1]NOAA/NGDC, Boulder Colorado

[2]University of Colorado, Boulder

[3]George Mason University, Fairfax Virginia

[4]University of Calgary, Calgary Alberta, Canada

Revised: June and August 2014

Abstract

The role of electron precipitation in the auroral zone in driving thermal O^+ upwelling is explored by comparison of observations and model results. Previous reports have shown how the ambiguities of such an assessment can be reduced when the problem is addressed in dynamic boundary related (DBRL) coordinates. Upwelling ion data from the DMSP satellites is compared using a modeling framework based on the Field Line Interhemispheric Plasma (FLIP) ionospheric model. We focus on geomagnetically quiet intervals, that is non-storm times with $D_{ST} > -50$ nT. We find that low energy (< 100eV) electrons are a significant driver of O^+ upwelling on the nightside, particularly in the 2100 MLT sector. Our analysis suggests that DMSP electron observations and electron precipitation models derived from them significantly underestimate the actual flux of soft (i.e. <100 eV) electrons.

Index terms:

Keywords: Ionospheric O^+ upwelling, soft electron precipitation, DMSP, Magnetosphere-Ionosphere coupling, Global models.

Three Key Points for the GEMS form.

1) Data and models of ion upwelling are compared.
2) Significant disagreement is found on the nightside.
3) Differences are attributed to underestimation of soft electron precipitation.

Introduction

The energization and transport of O^+ ions from the cold dense ionosphere to the magnetosphere has been under investigation for several decades. See for example Shelley et al., [1976], Chappell et al., [1987], Yau and Andre, [1997], Yau et al., [2007, 2011]. We now know that multiple processes are involved in energizing cold ionospheric O^+ to escape velocity. The first of these processes is the upwelling of the cold O^+ ionospheric ions into the upper thermosphere. Upwelling associated with the rapid onset of bulk field-aligned upward O^+ flux at sunrise at mid-latitudes driven by photoionization was discovered early in the space age [e.g., Evans, 1975, Redmon et al., 2012b]. Upwelling of O^+ was subsequently observed at auroral and polar cap latitudes at all local times [e.g. Loranc et al, 1991]. Upwelling at auroral

45 latitudes is the result of heating of the ionosphere by many processes including
46 photoionization, Joule heating, and particle precipitation [e.g. Burns et al., 2007]. In
47 particular, Seo et al., [1997] demonstrated strong correlations between ion
48 upwelling at altitudes ~900 km and precipitating electrons with energies below 80
49 eV. Modeling by Caton et al. [1996] and others demonstrated the importance of
50 electron precipitation at energies below 1 keV in heating the topside ionosphere and
51 subsequently creating ion upwelling. The purpose of this paper is to assess the
52 importance of soft electrons as captured in models of electron precipitation in
53 producing O^+ upwelling in the ionosphere.

54 Variation in O^+ upwelling rates and locations leads to temporal and spatial variability
55 of energetic O^+ in the magnetosphere (e.g. [Peterson et al., 2002]). Concentrations of O^+
56 in the magnetosphere change the Alfvén velocity, which has an impact on reconnection
57 rates (e.g., [Shay and Swisdak, 2004; Hesse and Birn, 2004]). These concentrations can
58 also modify the pressure distribution in the ring current, thus modifying the evolution of
59 large geomagnetic storms (e.g., [Brandt et al., 2002; Delcourt, 2002, Peterson et al., 2009,
60 Kistler et al., 2010]). Understanding the role of O^+ in these large-scale temporally and
61 spatially varying magnetospheric processes is challenging (e.g. [Lotko, 2007; Wiltberger,
62 2013]). The advent of multi-fluid MHD codes provides new tools for investigating the
63 impact of oxygen ions on the magnetosphere (e.g. [Winglee, 1998; Raeder et al., 2004;
64 Glocer et al., 2004; Ridley et al., 2009; Wiltberger et al., 2009, 2010]). O^+ upwelling and
65 energization is also modeled in thermospheric codes with magnetospheric coupling such
66 as the Field Line Inter-hemispheric Plasma model (FLIP, [Richards et al., 2001]),
67 Thermosphere-Ionosphere-Electrodynamics General Circulation Model (TIE-GCM,

68 [Qian et al., 2009]), and the Global Ionosphere Thermosphere Model (GITM, [Ridley et
69 al., 2006]). For a recent review of global simulations see Wiltberger [2013].

70 Global codes, such as those noted above, use various approaches to model and
71 validate energy input from precipitating electrons. Some codes use an empirical model
72 based on observations supplemented by the Knight [1973] relationship driven by
73 modeled magnetospheric parameters to estimate precipitation flux and characteristic
74 energy. Most codes use empirical models of electron precipitation. Validation of the
75 electron precipitation flux and characteristic energy used in these models is difficult and
76 not always discussed in the literature. The most common forms of validation use the
77 NOAA/POES global hemispheric power observations and/or the cross polar cap potential
78 derived from DMSP satellites. In some cases direct comparisons are made; in others
79 electron precipitation is used as a tuning parameter to optimize agreement with NOAA
80 hemispheric power and/or DMSP cross polar cap potentials. See for example, Ridley et
81 al., [2004], and Zhang et al., [2011].

82 Recently Redmon et al. [2012b] demonstrated that the well-known dawnward bias in
83 escaping energetic O^+ fluxes is the result of peak O^+ upwelling just after dawn [Evans,
84 1975] and noon focused energization mechanisms associated with the cusp. Redmon et al.
85 [2012b] compared observations of upwelling ions on Defense Meteorological Satellite
86 Program (DMSP) with models of the plasma on magnetic field lines as they moved in
87 and out of sunlight and regions of electron precipitation. Details of the modeling
88 framework that uses the FLIP code are given in Redmon et al., [2012b]. These
89 investigations were made in dynamic boundary related coordinates (DBRL), which
90 reduces ambiguities associated with the motion of the auroral zone in geographic

coordinates. The use of DBRL coordinates demonstrates the importance of the history of energy input on field lines as they move through local time. Redmon et al. [2012b] found that, on the dayside, electron precipitation plays a relatively minor role in driving upwelling O^+ ions except near noon, where it plays a supporting role. In this paper we extend the Redmon et al. [2012b] data/model comparison into the nightside, where the energy inputs are more variable, and not as focused as in the cusp region.

This paper is organized as follows. We review the observations of upwelling O^+ in dynamic boundary related coordinates and the model framework developed to investigate the importance of various energy sources driving upwelling. We then compare the data and model and discuss our results in terms of our current empirical understanding of the energy spectra of precipitating electrons.

Observations

Figure 1 presents upwelling O^+ observations from the Defense Meteorlogical Satellite Program (DMSP) satellites assembled and discussed by Redmon et al. [2010, 2012a, and 2012b]. It shows maps of the net upwelling number flux in dynamic boundary related coordinates (DBRL, left) and magnetic latitude vs magnetic local time (MLT, right). These data were obtained in the southern hemisphere from 1997 through 1998 during gemoagnetically quiet conditions (i.e during non-storm times when the D_{ST} index was greater than -50 nT). As noted by Redmon et al., [2012a] and many others, DMSP observations are sparse at post noon and post midnight local times. For the data/model

113 comparisons discussed below we have chosen to present the observations in eight 3-hr
114 MLT sectors and latitude bins as described below.

115 Loranc et al. [1991] and many others have demonstrated that the temporal variation
116 of up and down welling fluxes in the auroral zone is complex. It is not uncommon for
117 multiple regions alternately dominated by up and down welling ions to be encountered as
118 a satellite crosses the auroral zone and polar caps. Figure 2 presents a deeper view into
119 the components of net upwelling flux shown in Figure 1. We note that at the altitude of
120 DMSP the ions are dominantly O^+ at high latitudes. Figure 2 is divided into 8 sections,
121 each corresponding, and positioned according to a 3-hr MLT sector shown in Figure 1. In
122 each sector there are 4 line plots describing the variability of the observations that were
123 included in the average net upwelling fluxes reported in Figure 1.

124 The O^+ vertical fluxes are the product of velocities and densities obtained from the
125 Ion Drift Meter (IDM) and Retarding Potential Analyzer (RPA) instruments on the
126 DMSP spacecraft as described by Redmon et al., [2010]. The velocity is sampled at a rate
127 of 6 Hz. We use 4-second averages of the vertical component of velocity (v_z) and sample
128 deviations (σ_{vz}). To compute a measure of the statistical variability of the net upwelling
129 fluxes during quiet times, we assume that the density is smoothly varying over the 4
130 second integration period, which is consistent with the observation by Coley et al., [2003]
131 that "the most variation in velocity is seen around the level of the average ion density".
132 The 4-second *i-th* sample variance of O^+ flux (F_i) is then approximated as:

133 $$\sigma_{F_i}^2 \approx \overline{n_i}^2 \, \sigma_{v_{zi}}^2, \quad where \; F_i = \overline{n_i} \, \overline{v_{zi}} \qquad (1)$$

Then a computationally efficient flux deviation was computed by averaging and taking the square root of the individual velocity sample variances as follows:

$$\overline{\sigma_{F_i}} = \sqrt{\frac{1}{N}\sum_{i=1}^{N} \overline{n_i}^2 \, \sigma_{v_{zi}}^2} \qquad (2)$$

The top pair of plots in each of the 8 MLT sectors in Figure 2 show the log of the absolute value of mean upward and downward fluxes, respectively, plus or minus one relative standard deviation ($\overline{\sigma_{F_i}}$) as given in (2), as a function of latitude in dynamic boundary coordinates. Vertical dotted-dashed lines indicate the equatorward and dashed lines indicate the poleward boundaries of the auroral oval. The blue square identifies the middle of the auroral zone where probability distributions are computed and reported in the bottom pair of plots in each MLT sector.

The bottom pair of plots in each MLT sector show the occurrence distributions of upward (left) or downward (right) O^+ flux events in the middle of the auroral zone. The absolute value of the fluxes is reported in units of $\log_{10}$ (ions/m^2/s) on the horizontal axis in fifteen logarithmically spaced bins covering the flux range from 10^{10} to $10^{13.5}$ ions/m^2/s. This bin spacing guarantees that even the least sampled bin has in excess of 25 samples. Events whose flux was less than the first bin are added to that bin to retain the total count, such that the first bin represents the probability of events where |flux| < $10^{10.25}$ (ions/m^2/s). These low fluxes do not contribute significantly to the distribution plots. Because our data samples are limited to geomagnetically quiet times, no fluxes greater than $10^{13.5}$ ions/m^2/s were observed. The vertical axis shows the occurrence probability of a specific flux level such that the upward and downward distribution

155 probabilities sum to 100%. Each distribution depicts the most probable value (peak),
156 mean (dash) and median (dash-dot) of the samples. The mean and median are always
157 within 1 bin spacing and the mean and most probable are usually within 1 bin spacing
158 and always within 1.5 bins. Comparing the most probable, mean and median quantities
159 provides a measure of the symmetry and the statistical influence of outliers in the
160 underlying distribution.

161 The plots demonstrate that the probability distributions of net O^+ flux at various
162 magnetic local times in the middle of the auroral zone at DMSP altitudes can be
163 unimodal or bimodal. The probability of observing upward flowing O^+ flux events in the
164 day side hours of 9, 12, and 15 MLT (top three sectors) is much greater than the
165 probability of observing downward events – i.e. the net probability distribution is mostly
166 unimodal. This reflects the fact that during daylight the ionosphere is strongly driven by
167 near noon energization mechanisms (e.g. photoionization, soft particle precipitation and
168 Joule heating). The top left plots in these sectors show that the mean upward fluxes rise
169 (steeply for 12 MLT) in the anti-sunward / poleward direction, peaking just poleward of
170 the polar cap boundary. The top right plots demonstrate a similar rise in downward fluxes,
171 peaking poleward of the peak in upward fluxes. Redmon et al. [2012b] compared these
172 data to models and demonstrated that the well-known dawnward bias in escaping
173 energetic escaping O^+ fluxes is the combined result of peak O^+ upwelling just after dawn
174 and intense cusp region energization.

175 During magnetically quiet times, the probability of observing downward flux events
176 in the middle of the auroral zone is greatest in the nighttime hours (e.g. 21, 00, 03 MLT)
177 as shown in the bottom three sectors. At these hours, the probability of observing upward

178 fluxes is similar to the probability of observing downward fluxes – i.e. the net distribution
179 is bimodal. In the middle of the midnight auroral zone (middle bottom sector), the
180 probability of observing downward flux events exceeds that of observing upward flux
181 events by ~ 12%. However the mean and median of the upward flux in this hour slightly
182 exceeds that of the downward flux events as demonstrated both in the plots here and in
183 the mean net flux plot of Figure 1a. The upward mean (dashed) and median (dash-dot)
184 values exceed those of the downward fluxes. In the absence of photoionization, the
185 observed upwelling in the nighttime hours is dependent on other processes such as
186 particle precipitation and Joule heating.

187

188 ## Modeling

189

190 Several authors have shown that the softest precipitation is the most effective in their
191 energy deposition in the F-region [Rees, 1989] and the resulting production of upwelling
192 ions [Liu et al., 1995]. To further investigate the role of the energy spectrum of electron
193 precipitation in producing ion upwelling in dynamic boundary related (DBRL)
194 coordinates, we use the model framework described in Redmon et al. [2012b]. This
195 framework is based on the Field Line Interhemispheric Plasma model [FLIP, Richards,
196 2001, 2010], and it is implemented and its outputs are given in DBRL coordinates. The
197 FLIP model has been very successful at modeling the radar plasma measurements at
198 Poker Flat [Richards et al., 2009]. The model framework has options for including the
199 effects of neutral winds from the Horizontal Wind Model (HWM93, [Hedin et al., 1996])
200 and electron precipitation. The FLIP model is cast in geographic coordinates. The

location of a field line in the FLIP model can be specified by L-shell and magnetic longitude or geographic coordinates at 250km altitude. We use the most recent FLIP code that includes improvements in the way backscattered electrons are treated [Richards, 2013]. To convert from geographic to DBRL coordinates we used a grid of 40 flux tubes at 8 geographic longitudes and 5 geographic latitudes. In the model framework geographically fixed locations in the high latitude ionosphere move in and out of the auroral zone as the Earth rotates. We used the K_P=2 mapping of the auroral oval in geomagnetic coordinates determined by Feldstein [1963] and reported by Holzworth and Meng [1975].

Photoionization and electron precipitation inputs to the FLIP model vary as the flux tube rotates. The flux tubes were selected such that the final locations of the five latitudinal flux tubes in each longitudinal sector consisted of one flux tube in the polar cap, one equatorward of the auroral zone, and three within the auroral zone. Modest activity levels (K_P = 2, A_P = 7, and $F_{10.7}$ = 100) were used for the non-storm time DMSP data considered here. We modeled equinox conditions and chose the model input parameters so that the solar zenith angles in the ionosphere at 6 and 18 MLT are equal and near 90^o. Figure 3 shows the geographic latitude and longitude of one of the 40 flux tubes as a function of time. A sample single flux tube, which passes through 9 MLT at 0 UT, is shown here (green circle). Auroral precipitation is turned on when the flux tube is inside the Feldstein oval (red circles).

The FLIP model precipitating electron flux can be Gaussian or Maxwellian distributions that are specified by a characteristic energy and intensity [Richards, 1995]. Several empirical electron precipitation models derived from DMSP observations have

224 recently been reviewed by Newell et al., [2010a]. Here we use the Oval Variation,
225 Assessment, Tracking, Intensity, and Online Now casting (OVATION) Prime (OP)
226 model [Newell et al., 2009, 2010b] to determine the electron energy flux and
227 characteristic energy inputs in the modeling framework. The OP model provides the total
228 electron precipitation broken down into three components: diffuse, broadband, and mono-
229 energetic electron precipitation, which can be used as proxies for three different electron
230 precipitation processes. The characteristic energies and intensities derived from the OP
231 model are depicted in Figure 4. From top to bottom data for total, diffuse, broadband, and
232 mono-energetic characteristic energy (left) and precipitating electron energy flux (right)
233 are shown. In the characteristic energy maps black cells are cells with no coverage or for
234 which a statistically significant characteristic energy was not available. Grey indicates
235 characteristic energies above 1,000 eV. Diffuse precipitation dominates for the modest
236 geomagnetic activity levels considered here.

237 Figure 5 presents the results of model framework runs with no auroral input (Panel a)
238 and the four OP electron precipitation patterns shown in Figure 4 (Panels b-e). The
239 upwelling fluxes determined from the model framework are presented in dynamic
240 boundary related coordinates for comparison with the observations shown in Figure 1a.
241 In Figure 5 there is an artificial separation between the three auroral zone flux tubes and
242 flux tubes equatorward and poleward of it.

243 The observations in Figure 1a show upwelling on the nightside and in particular the
244 2100 MLT sector. Figure 5 shows that, in the 21 MLT sector, none of the OP
245 precipitation patterns considered in the modeling framework result in net upwelling
246 fluxes. A comparison of Figure 5a (no aurora) with the various auroral precipitation cases

247 (b) – (e) shows that quiet time auroral precipitation predicted by the OP model only
248 marginally influences the total upwelling O^+, with the most significant enhancement
249 occurring in the morning hours, realized by the diffuse (c) and total (b) precipitation
250 patterns. Redmon et al., [2010b] have compared the DMSP observations and model
251 framework results on the dayside. Here we focus on the nightside.

252 Joule heating and particle precipitation are the major energy sources driving
253 upwelling. The model framework used to produce Figure 5 includes the effects of
254 ionospheric convection and Joule heating indirectly, through the densities and
255 temperatures from the empirical Mass Spectrometer and Incoherent Scatter (MSIS,
256 http://en.wikipedia.org/wiki/NRLMSISE-00) model and winds determined from the
257 International Reference Ionosphere (IRI, http://iri.gsfc.nasa.gov/) model h_mF_2. Because
258 we are focusing on geomagnetically quiet intervals, we know that the effects of ion
259 frictional heating are modest. To estimate the level of ion frictional heating during
260 geomagnetically quiet conditions we use parameters derived from the Assimilative
261 Mapping of Ionospheric Electrodynamics (AMIE, Richmond, 1992) as a proxy for Joule
262 heating. Figure 6 (reproduced from Redmon et al., 2012a) presents simple Joule heating
263 (i.e. **J•E**) contours derived from the AMIE procedure for the non-storm conditions
264 considered here. It shows that the average quiet time Joule heating pattern is consistent
265 with the traditional 2-cell convection pattern where the average IMF By is 0. The heating
266 power is generally > 1 mW/m^2 above 65 degrees magnetic latitude with maxima of ~3
267 mW/m^2 at dawn, dusk and noon.

268 We note that the non-storm time average shown in Figure 6 does not include a peak
269 in Joule (ion-frictional) heating in the 2100 MLT sector where the observed nightside

upwelling is maximum. In fact, the energy input in the 2100 MLT sector from ion-frictional (Joule) heating suggested in Figure 6 has a local minimum in the 2100 MLT sector. The color bars in Figure 5 and the contours in Figure 6 are chosen to facilitate comparison of energy inputs into the ionosphere from electron precipitation and Joule heating. In the 2100 MLT sector, the energy available from quiet time Joule heating cannot explain all of the differences between observed (Figure 1) and modeled (Figure 5) upwelling using the OP electron precipitation model. Clearly more energy input is required in the nightside auroral zone, particularly in the 2100 MLT sector, to account for the upwelling ion flux observed on DMSP. This inconsistency motivates an investigation into model representations of the energy spectrum of precipitating electrons, particularly in the 2100 MLT sector.

It is conceivable that a significant portion of precipitating flux from electrons with energy below ~100 eV is unaccounted for in the standard models of electron precipitation derived from DMSP data (P. Newell, private communication). Andersson et al. [2002] and others have shown that dispersive Alfvén waves create downward beams of low energy electrons. Chaston et al., [2007] have shown that on the nightside dispersive Alfvén waves are commonly observed and associated with energetic ion outflows observed on the FAST satellite. DMSP electron observations and the OVATION Prime model cannot characterize electrons at the lowest (< 100 eV) characteristic energies [Newell et al., 2010a,b]. Due to uncertainties associated with limited instrument sensitivity below 100 eV and spacecraft charging effects, it is difficult to accurately account for the lowest energy (< 100 eV) precipitating electrons using only the DMSP data or the OP precipitation model.

293 To explore the relative importance of the low energy component of electron
294 precipitation we developed and describe below an alternative electron precipitation map
295 that, when used in the model framework, best fits the DMSP observations. Because the
296 present model framework does not explicitly consider ion convection, the alternative
297 electron precipitation map is useful only in exploring the idea that the under estimation of
298 the low-energy flux and resulting overestimation of the characteristic energy of
299 precipitating electrons in the OP model could account for the underestimation of O^+
300 upwelling in the 2100 MLT sector reported in Figure 5.

301 To facilitate the determination of a best-fit electron precipitation model, the model
302 framework was run using a series of constant auroral precipitation patterns with single
303 Maxwellian distributions for characteristic energies of 50, 100, 200 and 1000 eV at
304 power levels of 0.3 mW/m^2 and 100, 200 and 1000 eV at the power level of 1 mW/m^2.
305 The results of these model runs are displayed in Figure 7. Black squares with black
306 dashed lines in Figure 7 show the average DMSP observations reported in Figure 1(a).
307 The x-axis shows the position of the observations and modeled flux tubes relative to
308 auroral boundaries. Figure 7 focuses on upward directed fluxes. No data or model run
309 results are reported for downward directed ions.

310 Figure 7 clearly demonstrates that the lowest energy (softest) precipitation is the
311 most effective in producing upwelling ions. For example, the case of 0.3 mW/m^2 in
312 energy flux and 50 eV in characteristic energy (yellow pluses) is nearly as effective at
313 producing upwelling fluxes at all MLTs as the case of 1 mW/m^2 energy flux and 200 eV
314 characteristic energy (red squares). The model results without precipitation (green pluses)
315 are given for 5 latitudes (one point in the middle of the auroral zone, points at the

316 equatorward and poleward auroral boundaries, and points at latitudes above and
317 below the auroral boundaries). In the middle of the auroral zone from 9 to 18 MLT the
318 model without precipitation agrees well in magnitude with the DMSP observations (black
319 squares). This confirms the result of Redmon et al., [2012b] that only modest
320 precipitation is required for the model to be in agreement with statistical observations on
321 the dayside. In the nightside auroral zone, however, another energy source in the model
322 framework is required to reproduce the observed upwelling O^+ flux. The estimates of
323 heating shown in Figures 6 and 7 suggest that the extra energy could come from low
324 energy (< 100 eV) electron precipitation not captured in the OP electron precipitation
325 model.

326 The data shown in Figure 7 were used to develop a single Maxwellian precipitating
327 electron precipitation pattern that, when used in the model framework, yielded upwelling
328 ions that qualitatively best matched the average observations. To create a best-fit
329 precipitation pattern we segmented the Feldstein oval into 3 latitudes and 8 local time
330 bins. In each of these 24 bins, we chose a single Maxwellian precipitating electron
331 population specified by its characteristic energy and energy flux. The new energy flux
332 was required to be within a factor of two of that given by the total electron precipitation
333 given by the OVATION Prime shown in the top panels of Figure 4. Where significant
334 upwelling was needed to match observations, lower characteristic energies than those
335 given by OP were used. The resulting precipitation map obtained after several iterations
336 is shown in Figure 8.

337 The characteristic energy in the 2100 MLT sector in Figure 8 is remarkably lower
338 than those given by the four versions of the OP maps model shown in Figure 4. In all
339 local time sectors, the electron energy flux is about half of that given by the OP model.

340 Figure 9 shows the upwelling computed in the model framework using the electron
341 precipitation map shown in Figure 8. The map shown in Figure 9 is in general but not
342 perfect agreement with the observed upwelling fluxes in the auroral zone shown in Figure
343 1a. Figure 10 presents more detailed data illustrating the differences between the
344 framework maps derived using OP and best-fit precipitation maps and DMSP
345 observations. As noted above because the model framework does not explicitly consider
346 ion convection, the data in Figures 9, 10, and 11 below is useful only in exploring the
347 effects of under estimation of the flux of soft precipitating electrons in the OP model. We
348 note that modeling the auroral zone is challenging because the inputs are dynamic. Even
349 if the model contained every physical process, there would still be uncertainties due to
350 the intrinsic uncertainties in the magnitude and time evolution of convection patterns,
351 precipitation patterns, neutral densities, etc. See for example Goodwin et al., [2014].

352 Figure 11 compares the observed integrated fluence in 8 DBLR magnetic local time
353 sectors, with values calculated from the model framework with the best-fit precipitation
354 pattern and with no precipitation, respectively. Figure 11 demonstrates that the observed
355 magnetic local time distribution of upwelling O^+ in the auroral zone during
356 geomagnetically quiet times can be obtained in our modeling framework if we assume
357 that the OP electron precipitation model underestimates the fluxes of precipitating low
358 energy (< 100 eV) electrons. Global magnetospheric models, such as that presented

by Brambles et al., [2013] often compare calculated and observed total outflow rates to validate their models. Figure 11 illustrates the power of such comparisons.

Summary and Discussion

This assessment of the global role of soft electrons in driving ion upwelling was motivated by inconsistencies between observed and modeled upwelling fluxes on the nightside revealed in Redmon et al., [2012b]. Redmon et al. [2010, 2012a, and 2012b] and others have demonstrated that many of the ambiguities associated with auroral observations and modeling can be eliminated if the analysis is done in dynamic boundary related (DBRL) coordinates. A model framework based on the FLIP code [Richards, 2001, 2010, 2013] is used to model the effects of variations in solar EUV and electron precipitation energy input to the auroral zone as it moves in geographic coordinates with the Earth's rotation.

We have compared and contrasted global maps of observed O^+ upwelling during geomagnetically quiet times [Redmon et al., 2010a] with those obtained from the model framework in DBRL coordinates. Redmon et al. [2012b] focused on dayside upwelling fluxes; here we focus on the nightside. Figure 1 shows that, on average, the net flux of thermal O^+ ions observed on the DMSP satellites is upward at all local times. Figure 2 shows that the average flux on the nightside is the result of bi-modal distributions of upwelling and down flowing fluxes. Significant differences were found on the nightside of the auroral zone between the observations and the model framework, when using the

381 OVATION Prime (OP, Newell et al., 2010b) electron precipitation maps shown in Figure
382 4; Figure 5 illustrates the discrepancies to be particularly important in the 2100 MLT
383 sector where the model framework consistently shows no upwelling O^+ ions.

384 We focus on geomagnetically quiet intervals, that is non-storm times with $D_{ST} > -50$
385 nT. During storm times, significantly more energy is input to the ionosphere and its
386 distribution in intensity, local time, latitude, and altitude is most likely different than it is
387 during non-storm times. Figure 7 shows that ion frictional (Joule) heating of the
388 ionosphere during non-storm conditions is not particularly intense in the 2100 MLT
389 sector. The OP precipitation model shows relatively more intense, mono-energetic and
390 diffuse electron precipitation in the 2100 MLT sector during quiet times, but as can be
391 seen from the comparison of maps in Figures 4 and 6 the OP prediction of precipitating
392 flux is lower than that estimated for Joule heating. Because DMSP data are relatively
393 sparse in the post midnight sector, we focus our analysis on the MLT sector centered on
394 2100 MLT.

395 In the 2100 MLT sector, electron precipitation and Joule heating are the two major
396 sources of energy heating the ionosphere. In the discussion of Figure 6 above we
397 explored the possibility that a significant quantity of the soft precipitating electron flux is
398 unaccounted for in models of electron precipitation derived from DMSP data. We also
399 noted the limitations of the DMSP data and OP models derived from it to accurately
400 capture the intensity of low energy (< 100 eV) precipitating electrons. Figure 7
401 demonstrates that electron precipitation with a characteristic energy less than 100 eV is
402 more efficient in producing ion upwelling than precipitation with the same energy flux

403 but with a characteristic energy greater than 100 eV. Strangeway et al. [2005] and others
404 have also demonstrated this fact using different data and models.

405 To assess the importance of low energy electron precipitation in driving O^+
406 upwelling in the nightside in general and the 2100 MLT sector in particular, we explored
407 how much we would have to modify the characteristic energy and fluxes in the OP model
408 to obtain upwelling fluxes comparable to those observed and reported in Figure 1. A
409 modified electron precipitation pattern, shown in Figure 8, was found that when used in
410 the model framework gives a best fit to the upwelling fluxes seen in Figure 1. Figure 11
411 illustrates the good agreement between upwelling fluxes computed using the best-fit
412 precipitation map in the model framework.

413 The characteristic energy in the 2100 MLT sector in Figure 8 is remarkably lower
414 than those given by the four versions of the OP maps model shown in Figure 4. This
415 demonstrates that low energy (< 100eV) electrons are a significant driver of O^+ upwelling
416 on the nightside, particularly in the 2100 MLT sector. It also suggests that DMSP
417 electron observations and electron precipitation models derived from them systematically
418 underestimate the actual flux of <100 eV electrons.

419 Because the model framework does not explicitly consider ion convection, the
420 electron precipitation map is useful only in the context of exploring if under estimation of
421 the characteristic energy of precipitating low energy electrons in the OP model accounts
422 for a portion of the underestimation of O^+ upwelling in the 2100 MLT. More detailed
423 modeling that includes convection is required to estimate the relative importance of soft
424 electrons and Joule heating in driving nightside O^+ upwelling.

425 Understanding the role of O^+ in large-scale temporally and spatially varying
426 magnetospheric processes is challenging. Peterson et al., [2009], Yau et al., [2012], and
427 others have shown that the magnitude of O^+ fluxes in the pipe line between the
428 ionosphere and plasma sheet at non-storm times is significant and could have a large
429 impact on magnetospheric dynamics. As noted in the introduction, validation of the
430 energy sources driving O^+ upwelling and outflow, particularly soft electron precipitation,
431 in global scale codes is difficult and not always discussed in the literature. The results
432 here suggest that the role of soft electrons in driving upwelling and subsequent outflow in
433 the nightside during non-storm times is not adequately captured in global models that
434 include O^+ transport. In particular the lack of verifiable quantitative information about
435 variation in magnetic local time of ion upwelling driven by soft electrons means that it is
436 not possible to determine the relative day and nightside fluxes of upwelling and escaping
437 O^+ with the precision needed to make advances in our understanding of the role of O^+ in
438 magnetospheric dynamics.

439

440 ## Conclusion
441

442 We have compared observations and models of upwelling O^+ fluxes in dynamic
443 boundary related coordinates (DBRL) using various maps of electron precipitation. The
444 comparison is made for geomagnetically quiet, non-storm times characterized by the D_{ST}
445 index greater than -50 nT.

446 We found that low energy (< 100eV) electrons are a significant driver of O^+
447 upwelling on the nightside and in particular the 2100 MLT sector. Our results suggest
448 that DMSP electron observations and electron precipitation models derived from them
449 significantly underestimate the actual flux of <100 eV electrons.

450 Global models used to explore the role of O^+ in magnetospheric processes have not
451 yet addressed the implications of a systematic underestimation of low energy electron
452 precipitation and subsequent underestimation of ion upwelling on their results. Our
453 results suggest that such an investigation could lead to new insights into the complex role
454 of O^+.

455

456 ## Acknowledgements
457

458 Thanks to Patrick Newell and Mike Wiltberger for helpful conversations. WKP was
459 supported by NASA Grant NNX12AD25G. AWY was supported by the Canadian Space
460 Agency and the Natural Science and Engineering Research Council Industrial Research
461 Chair Program. PGR was supported by NSF grant AGS-1048350 to George Mason
462 University. DMSP Special Sensor for Ions Electrons and Scintillation (SSIES) data were
463 acquired from a University of Texas at Dallas public repository:

464 http://cindispace.utdallas.edu/DMSP/

465

466

References

Andersson, L., W.K. Peterson and K.M. McBryde (2004), Dynamic coordinates for auroral ion outflow, J. of Geophys. Res., 109(A8), doi:10.1029/2004JA010424.

Andersson, L., N. Ivchenko, J. Clemmons, A. A. Namgaladze, B. Gustavsson, J.-E. Wahlund, L. Eliasson, and R. Y. Yurik (2002), Electron signatures and Alfvén waves, J. Geophys. Res., 107(A9), 1244, doi:10.1029/2001JA900096.

Brambles, O. J., W. Lotko, B. Zhang, J. Ouellette, J. Lyon, and M. Wiltberger (2013), The effects of ionospheric outflow on ICME and SIR driven sawtooth events, J. Geophys. Res. Space Physics, 118,6026–6041, doi:10.1002/jgra.50522.

Brandt, P. C:son, S. Ohtani, D. G. Mitchell, M.-C. Fok, E. C. Roelof, and R. Demajistre (2002), Global ENA observations of the storm mainphase ring current: Implications for skewed electric fields in the inner magnetosphere, Geophys. Res. Lett., 29(20), 1954, doi:10.1029/2002GL015160.

Burns, A.G, S.C. Colomon, W. Wang, and T.L. Kileen (2007), The ionospheric and thermospheric response to CMEs: Challenges and successes**, J. Atmos. And Solar-Terr. Phys., 69, 77, doi:** 10.1016/j.jastp.2006.06.010.

Caton, R., J. L. Horwitz, P. G. Richards, and C. Liu (1996), Modeling of F-region ionospheric upflows observed by EISCAT, Geophys. Res. Lett. 23, 1537, doi:

Chappell, C. R., T. E. Moore, and J. H. Waite Jr. (1987), The ionosphere as a fully adequate source of plasma for the Earth's magnetosphere, J. Geophys. Res., 92, 5896-5910.

Chaston, C. C., C. W. Carlson, J. P. McFadden, R. E. Ergun, and R. J. Strangeway (2007), How important are dispersive Alfve´n waves for auroral particle acceleration?, Geophys. Res. Lett., 34, L07101, doi:10.1029/2006GL029144.

Coley, W. R., R. A. Heelis, and M. R. Hairston (2003), High-latitude plasma outflow as measured by the DMSP spacecraft, J. Geophys. Res., 108(A12), 1441, doi:10.1029/2003JA009890.

Delcourt, D. C. (2002), Particle acceleration by inductive electric fields in the inner magnetosphere, J. Atmos. Sol. Terr. Phys., 64, 551.

Evans, J. V. (1975), A study of F2 region daytime vertical ionization fluxes at Millstone Hill during 1969, Planetary and Space Science, 23, 1461–1482, doi:10.1016/0032-0633(75)90001-X.

Feldstein, Y. (1963), Some problems concerning the morphology of auroras and magnetic disturbances at high latitudes, *Geomagnetism and Aeronomy*, 3, 183.

503 Glocer, A., G. Tóth, Y. Ma, T. Gombosi, J.-C. Zhang, and L. M.
504 Kistler (2009), Multifluid Block-Adaptive-Tree Solar wind Roe-type Upwind
505 Scheme: Magnetospheric composition and dynamics during geomagnetic storms—
506 Initial results, J. Geophys. Res., 114, A12203, doi:10.1029/2009JA014418.

507 Goodwin, L., J.-P. St.-Maurice, P. Richards, M. Nicolls, and M.
508 Hairston (2014), *F* region dusk ion temperature spikes at the equatorward edge of the
509 high-latitude convection pattern, Geophys. Res. Lett.,41, 300–307,
510 doi:10.1002/2013GL058442.

511 Hardy, D. A., E. G. Holeman, W. J. Burke, L. C. Gentile, and K. H. Bounar (2008),
512 Probability distributions of electron precipitation at high magnetic latitudes, J.
513 Geophys. Res., 113, A06305, doi:10.1029/2007JA012746.

514 Hedin, A. E., et al. (1996), Empirical wind model for the upper, middle, and lower
515 atmosphere, J. Atmos. Terr. Phys., 58, 1421–1447, doi:10.1016/0021-
516 9169(95)00122-0.

517 Hesse, M., and J. Birn (2004), On the cessation of magnetic reconnection, Ann. Geophys.,
518 22, 603– 612, www.ann-geophys.net/22/603/2004/.

519 Holzworth, R. H., and C.-I. Meng (1975), Mathematical representation of the auroral oval,
520 Geophys. Res. Lett., 2, 377–380, doi:10.1029/GL002i009p00377.

521 Kistler, L. M., C. G. Mouikis, B. Klecker, and I. Dandouras (2010), Cusp as a source for
522 oxygen in the plasma sheet during geomagnetic storms, *J. Geophys. Res.*, *115*, 03209,
523 doi:10.1029/2009JA014838.

524 Knight, S. (1973), Parallel electric fields, Planet. Space Sci., 21, 741.

525 Liu, C., Horwitz, J.L., Richards, P.G., (1995), Effects of frictional ion heating and soft-
526 electron precipitation on high-latitude F- region upflows. Geophysical Research
527 Letters 22, 2713–2716.

528 Lockwood, M., M. Chandler, J. Horwitz, J. Waite Jr., T. Moore, and C. Chappell (1985),
529 The Cleft Ion Fountain, J. Geophys. Res., 90(A10), 9736-9748.

530 Loranc M, Hanson WB, Heelis RA, St-Maurice JP (1991) A morphological study of
531 vertical ionospheric flows in the high-latitude F region. J Geophys Res 96:3627–
532 3646, doi:????

533 Lotko, W. (2007), The magnetosphere–ionosphere system from the perspective of plasma
534 circulation: A tutorial, J. Atmos. Sp. Phys., 69, 199.

535 Newell, P. T., T. Sotirelis, and S. Wing (2009), Diffuse, monoenergetic, and broadband
536 aurora: The global precipitation budget, J. Geophys. Res., 114, A09207,
537 doi:10.1029/2009JA014326.

538 Newell, P. T., T. Sotirelis, K. Liou, A. R. Lee, S. Wing, J. Green, and R.
539 Redmon (2010a), Predictive ability of four auroral precipitation models as evaluated

using Polar UVI global images, *Space Weather*, *8*, S12004, doi:10.1029/2010SW000604.

Newell, P. T., T. Sotirelis, and S. Wing (2010b), Seasonal variations in diffuse, monoenergetic, and broadband aurora, J. Geophys. Res., 115, A03216, doi:10.1029/2009JA014805.

Peterson, W.K., H.L. Collin, M. Boehm, A.W. Yau, C. Cully, and G. Lu (2002), Investigation into the Spatial and Temporal Coherence of Ionospheric Outflow on January 9-12, 1997, J. Atmos. and Solar Terr. Phys., 64, 1659, 2002.

Peterson, W. K., L. Andersson, B. C. Callahan, H. L. Collin, J. D. Scudder, and A. W. Yau (2008), Solar-minimum quiet time ion energization and outflow in dynamic boundary related coordinates, J. Geophys. Res., 113, A07222, doi:10.1029/2008JA013059.

Peterson, W.K., L. Andersson, B. Callahan, S.R. Elkington, R.W. Winglee, J.D. Scudder, and H.L. Collin (2009), Geomagnetic activity dependence of O^+ in transit from the ionosphere,*J. Atmos. Solar-Terr. Phys.*, 71, 1623, doi:10.1016/j.jastp.2008.11.003.

Qian, L., S. C. Solomon, and T. J. Kane (2009), Seasonal variation of thermospheric density and composition, J. Geophys. Res., 114, A01312, doi:10.1029/2008JA013643.

Raeder, J., D. Larson, Wenhui Li, E.I. Kepko, and T. Fuller-Rowell (2004), OpenGGCM Simulations for the THEMIS Mission, Sp. Sci. Rev. 141, 535, doi: 10.1007/s11214-008-9421-5

Redmon, R. J., W. K. Peterson, L. Andersson, E. A. Kihn, W. F. Denig, M. Hairston, and R. Coley (2010), Vertical thermal O+ flows at 850 km in dynamic auroral boundary coordinates, J. Geophys. Res., 115, A00J08, doi:10.1029/2010JA015589.

Redmon, R. J., W. K. Peterson, L. Andersson, and W. F. Denig (2012a), A global comparison of O^+ upward flows at 850 km and outflow rates at 6000 km during nonstorm times, J. Geophys. Res., 117, A04213, doi:10.1029/2011JA017390.

Redmon, R. J., W. K. Peterson, L. Andersson, and P. G. Richards (2012b), Dawnward shift of the day side O^+ outflow distribution: The importance of field line history in O^+ escape from the ionosphere, J. Geophys. Res., 117, A12222, doi:10.1029/2012JA018145.

Rees, M. H. (1989), Physics and chemistry of the upper atmosphere, Cambridge University Press, Cambridge

Richards, P. G. (1995), Effects of auroral electron precipitation on topside ion outflows, in Cross-Scale Coupling in Space Plasmas, Geophys. Monogr. Ser., vol. 93, edited by J. L. Horwitz, pp. 121–126, AGU, Washington, D. C.

576 Richards, P. G. (2001), Seasonal and solar cycle variations of the ionospheric peak
577 electron density: Comparison of measurement and models, J. Geophys. Res., 106,
578 12,803, doi:10.1029/2000JA000365.

579 Richards, P. G., M. J. Nicolls, C. J. Heinselman, J. J. Sojka, J. M. Holt, and R. R. Meier
580 (2009), Measured and Modeled Ionospheric densities, temperatures, and winds
581 during the IPY, *J. Geophys. Res.*, 114, A12317, doi:10.1029/2009JA014625

582 Richards, P. G., R. R. Meier, and P. J. Wilkinson (2010),On the consistency of satellite
583 measurements of thermospheric composition and solar EUV irradiance with
584 Australian ionosonde electron density data, J. Geophys. Res., 115, A10309,
585 doi:10.1029/2010JA015368.

586 Richards, P.G, (2013), Reevaluation of thermosphere heating by auroral electrons, Adv.
587 Sp. Res., 51, 610, doi: 10.1016/j.asr.2011.09.004.

588 Richmond, A. D. (1992), Assimilative Mapping of Ionosphere Electrodynamics,
589 Advances in Space Research, Volume 12, Issue 6, 1992, Pages 59-68, ISSN 0273-
590 1177, DOI: 10.1016/0273-1177(92)90040-5.

591 Ridley, A.J., T. I. Gombosi, and D. L. DeZeeuw (2004), Ionospheric control of the
592 magnetosphere: Conductance, Annal. Geophys. 22, 561.

593 Ridley, A. J., Y. Deng, and G. Tóth (2006), The global ionosphere–thermosphere model,
594 *J. Atmos. Solar Terr. Phys.*, *68*(8), 839–864, doi:10.1016/j.jastp.2006.01.008.

595 Roble, R.G., and M.H. Rees (1977), Time-dependent studies of the aurora: Effects of
596 particle precipitation on the dynamic morphology of ionospheric and atmospheric
597 properties, Planetary and Sp. Sci., 25, 991, doi: 10.1016/0032-0633(77)90146-5.

598 Seo Y, J.L. Horwitz, and R. Caton (1997) Statistical relationship between high-latitude
599 ionospheric F-region/topside upflows and their drivers: DE-2 observations. J
600 Geophys Res 102(A4):7493–7500

601 Shay, M. A., and M. Swisdak (2004), Three-species collisionless reconnection: Effect of
602 O^+ on magnetotail reconnection, Phys. Rev. Lett., 93, 175001,
603 doi:10.1103/PhysRevLett.93.175001.

604 Shelley, E.G. R.D. Sharp, and R.G. Johnson (1976), Satellite observations of an
605 ionospheric acceleration mechanism. Geophysical Research Letters, 3: 654–656.
606 doi: 10.1029/GL003i011p00654.

607 Strangeway, R.J., Ergun, R.E., Su, Y., Carlson, C.W., and Elphic, R.C. (2005), Factors
608 controlling ionospheric outflows as observed at intermediate altitudes, J. Geophys.
609 Res., 110, A03221, doi:10.1029/2004JA010829.

610 Winglee, R. (1998), Multi-fluid simulations of the magnetosphere: The identification of
611 the geopause and its variation with IMF, Geophys. Res. Lett. 25, 4441, doi:
612 10.1029/1998GL900217.

613 Wiltberger, M., R. S. Weigel, W. Lotko, and J. A. Fedder (2009), Modeling seasonal
614 variations of auroral particle precipitation in a global-scale magnetosphere-
615 ionosphere simulation, J. Geophys. Res., 114, A01204, doi:10.1029/2008JA013108

616 Wiltberger, M., W. Lotko, J. G. Lyon, P. Damiano, and V. Merkin (2010), Influence of
617 cusp O^+ outflow on magnetotail dynamics in a multifluid MHD model of the
618 magnetosphere, J. Geophys. Res., 115, A00J05, doi:10.1029/2010JA015579.

619 Wiltberger, M, (2013), Review of global simulation studies of the effect of ionospheric
620 outflow on the magnetosphere-ionosphere system dynamics, To appear in J.
621 Geophys. Res.

622 Yau, A.W., and M. André (1997), Sources of ion outflow in the high latitude ionosphere,
623 Space. Sci. Rev., 80, 1-25, doi: 10.1023/A:1004947203046.

624 Yau, A.W., T Abe, and W.K. Peterson (2007), The polar wind: Recent observations, J.
625 Atmos. And Solar Terr. Phys., 69, 1936, doi:10.1016/j.jastp.2007.08.010.

626 Yau, A.W., W.K. Peterson, and T. Abe (2011), Influences of the Ionosphere,
627 Thermosphere, and Magnetosphere on Ion Outflows, Article in "The Dynamic
628 Magnetosphere," W. Liu, and M. Fujimoto (eds.) IAGA Special Sopron Book Series
629 3, doi:10.1007/978-94-007-0501-2_16, Springer, p283, 2011.

630 Yau, A. W., A. Howarth, W. K. Peterson, and T. Abe (2012), Transport of thermal-
631 energy ionospheric oxygen (O^+) ions between the ionosphere and the plasma sheet
632 and ring current at quiet times preceding magnetic storms, J. Geophys. Res., 117,
633 A07215, doi:10.1029/2012JA017803.

634 Zhang, B., W. Lotko, M.J.Wiltberger, O.J.Brambles, and P.A.Damiano (2011), A
635 statistical study of magnetosphere-ionosphere coupling in the Lyons-Fedder-
636 Mobarry global MHD model, J. Atmos. and Solar Terr. Phys. 73, 686.

637

Figures

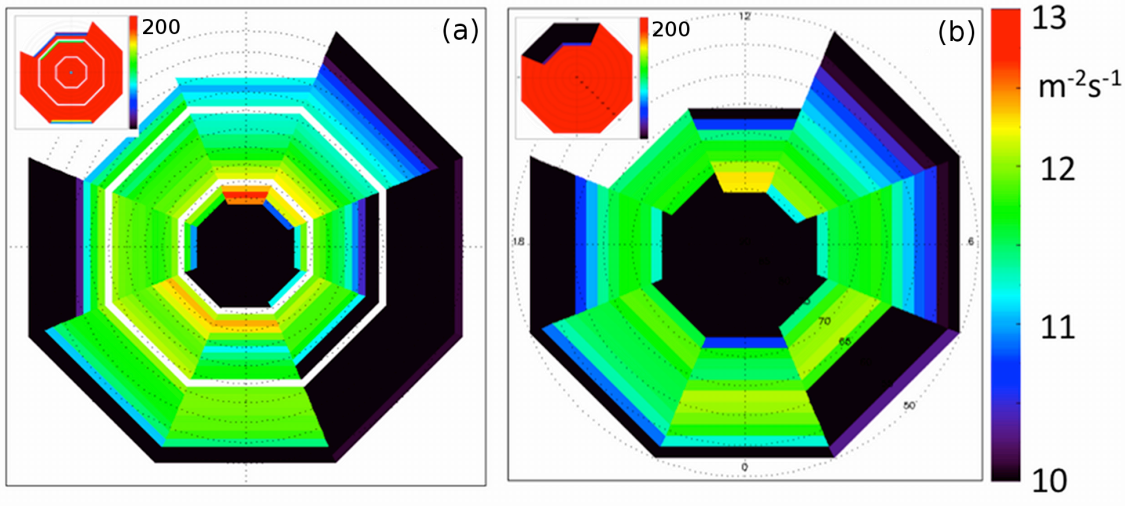

Figure 1: Vertical net number fluxes of O^+ (#/m^2/s) observed by DMSP near 850 km during geomagnetical quiet, non-storm conditions. Data are presented in (a, left) dynamic boundary related coordinates (DBRL, Redmon et al., 2010) and (b, right) magnetic latitude from 50^o to 90^o vs. magnetic local time (MLT). Noon (1200) is at the top and dawn (0600) is on the right of each dial. The white bands in (a) indicate the poleward and equatorward auroral boundaries. The smaller inset maps represent the number of samples in a given cell. Flux intensity and the number of samples are shown by the respective color bars.

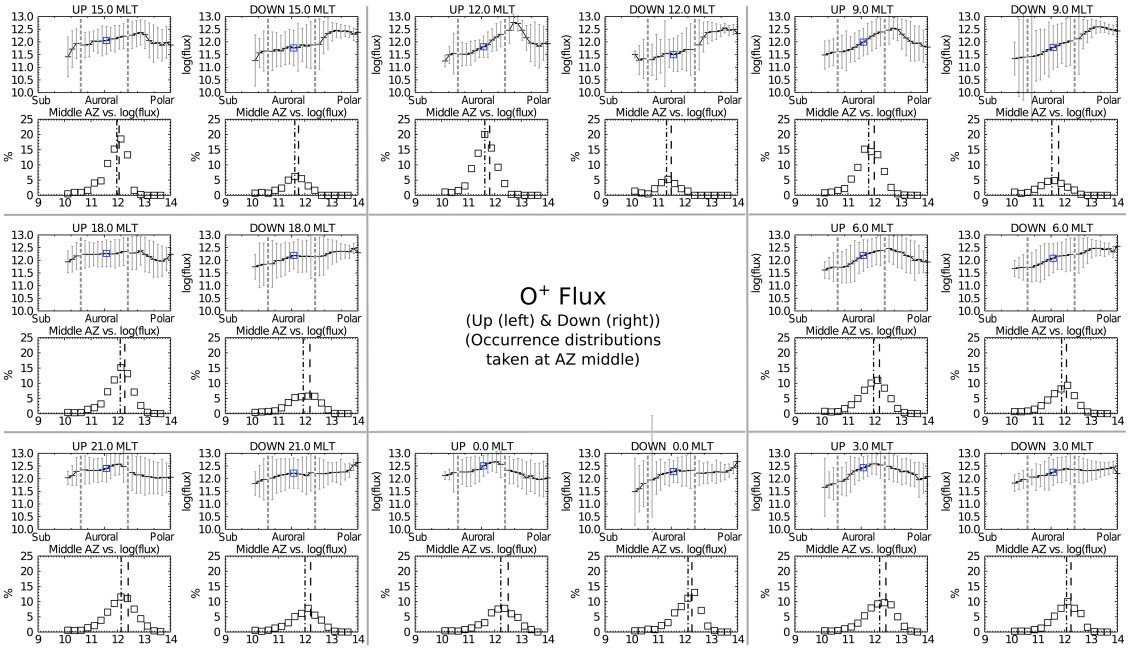

Figure 2: Dynamic boundary related coordinate plots of O^+ vertical ion flux and occurrence distributions observed by DMSP in each of the 8 MLT sectors represented in Figure 1. Top row, middle section: noon; middle row, right section: dawn; top panels in each sector: mean upward (left) and downward (right) vertical fluxes ±1 relative standard deviation in $\log_{10}$ (ions/m^2/s) versus the relative position within the auroral zone, from the sub-auroral region through the auroral zone to the polar cap (left to right), the middle of the auroral zone is indicated by a blue square; bottom panels: upward (left) and downward (right) O^+ occurrence distributions in the middle of the auroral zone (AZ) versus $\log_{10}$ of ion flux, and their mean (dash) and median (dash-dot).

661

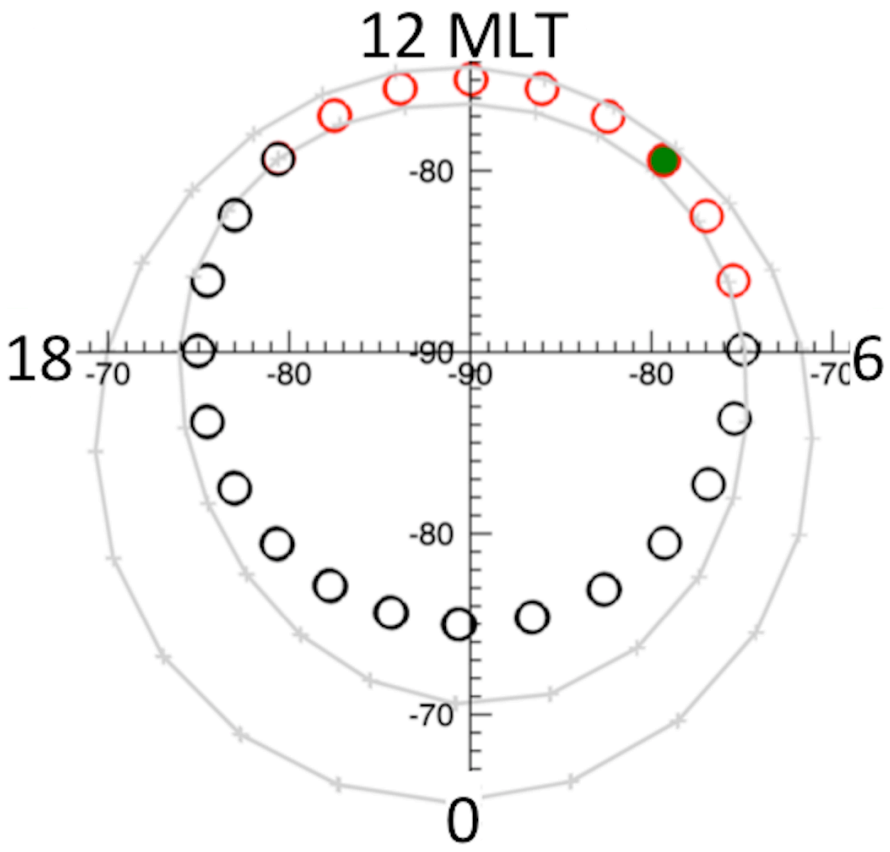

662

663 Figure 3: Example of the location (geomagnetic latitude and MLT) of a flux tube, which
664 is fixed in geographic coordinates and passes through the middle of the auroral zone at 9
665 MLT (green circle), relative to the auroral oval for 24 hours. The Feldstein auroral oval
666 for K_P =2 is shown in solid grey lines. The location of the flux tube is indicated by open
667 circles, which are colored red when the flux tube is in the auroral oval. The model
668 framework includes 40 flux tubes.

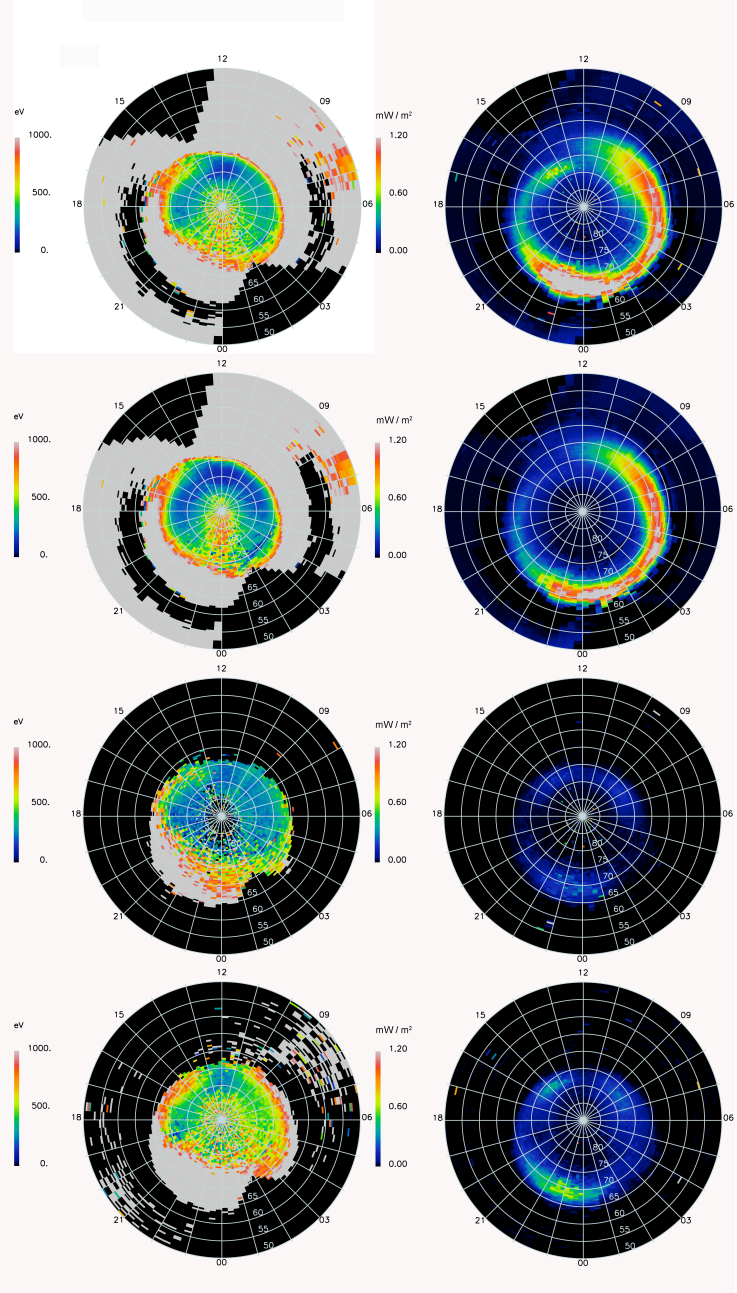

669

670

671 Figure 4: Maps of precipitating electron energy flux (right) and characteristic energy
672 (left) from the OVATION Prime model for low solar wind driving conditions. Top to
673 bottom: total, diffuse, broadband, and mono-energetic precipitation. Common color bars
674 are used to linearly encode characteristic energy from 0 eV to 1 keV and energy flux
675 covering the range from 0 to 1.2 mW/m^2. Black denotes no coverage or a statistically
676 insignificant value. Grey denotes energy or energy flux above the top limit of the color
677 bar. Dial plots are oriented with noon MLT on the top and dawn on the right. The lowest
678 (most equatorward) latitude is -50^o.

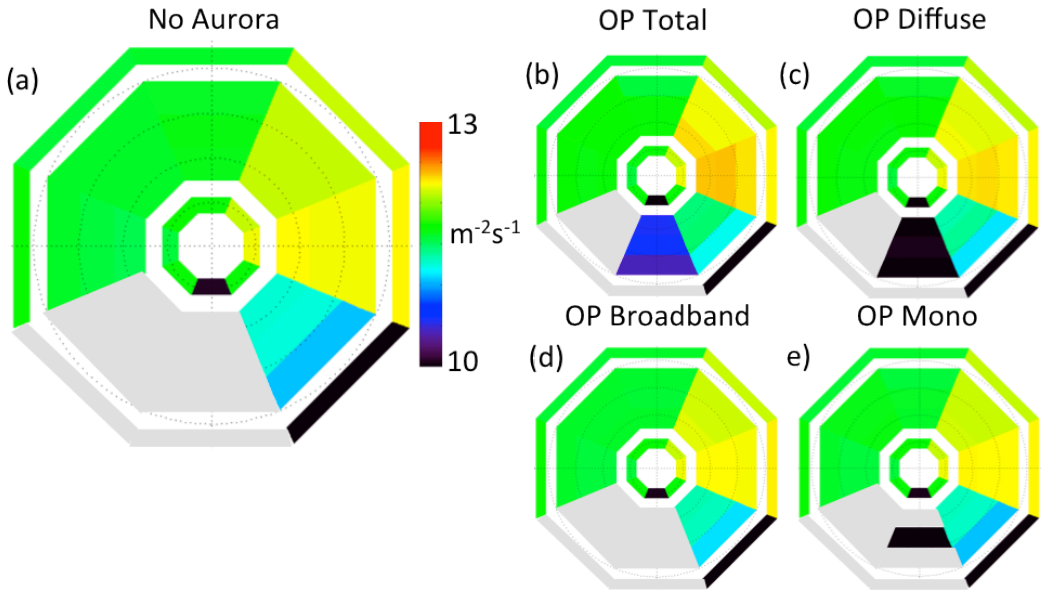

679

680 Figure 5: Modeled O^+ upwelling fluxes under the influence of various electron
681 precipitation patterns: (a) no electron precipitation applied, and (b) total, (c) diffuse, (d)
682 broadband, and (e) monoenergetic precipitation. All dial plots are oriented with noon
683 MLT on the top and dawn on the right. Upwelling ion flux at 850 km is encoded in
684 logarithm units using the color bar, which covers the range of flux 10^{10} – 10^{13} $m^{-2}s^{-1}$.
685 Cells colored grey indicate downwelling fluxes. The modeled flux tubes equatorward of,
686 inside, and poleward of the auroral zone are separated by the white bands.

687

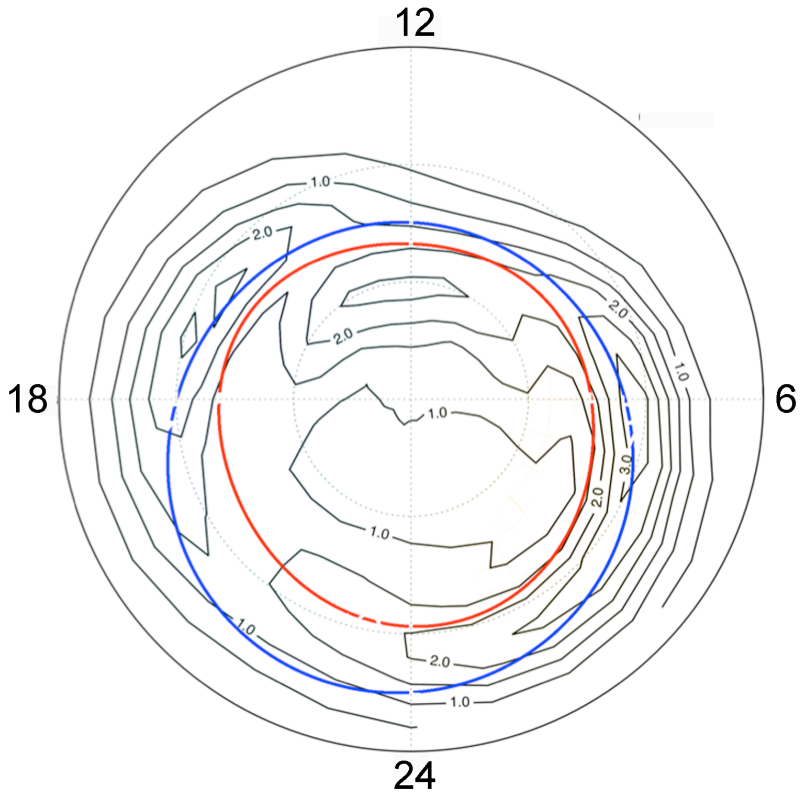

688

689 Figure 6: Reproduced from Redmon et al., [2012a]. Joule heating power (black contours
690 in units of mW/m^2) from average of 1-minute non-storm time AMIE model output for the
691 northern hemisphere in 1997-1998, and Feldstein oval for Kp=2 (blue and red lines), in
692 magnetic coordinates above 60°.

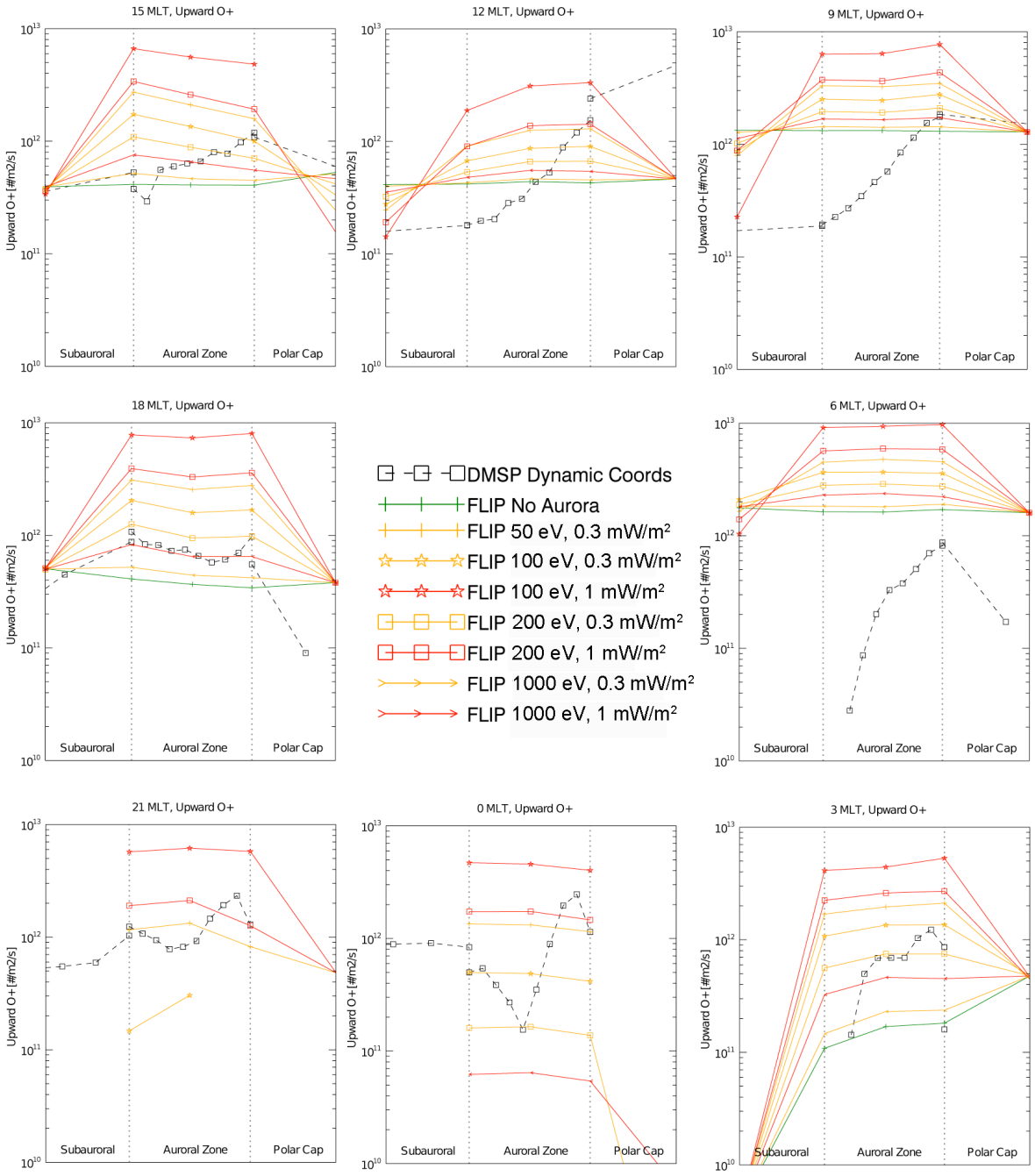

693

694 Figure 7: Comparison of observed and modeled upwelling O^+ fluxes at 850 km in the
695 southern hemisphere in DBRL coordinates for each of 8 MLT sectors (noon on the top
696 and dawn on the right). The grey vertical lines show the equatorward edge (left) and
697 poleward edge (right) of the auroral zone. The key in the center relates the symbols and
698 colored lines to the indicated parameters used in model runs. The black squares reproduce
699 DMSP observations shown in Figure 1(a). Net downward directed fluxes, indicated in
700 Figures 2 and 5, are not reported.

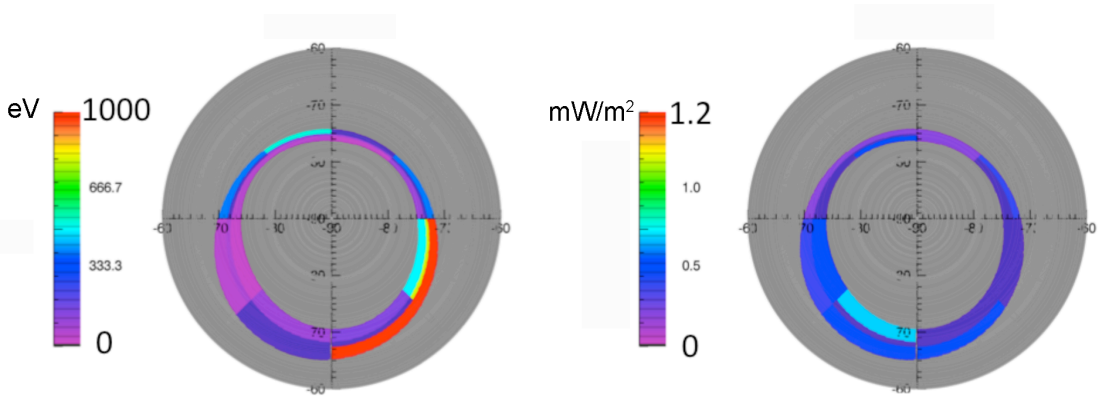

Figure 8: Maps of modeled precipitating electron characteristic energy (left) and energy flux (right), based on single characteristic energy Maxwellian distributions chosen to best fit the observed upwelling O^+ flux when used in the model framework, for magnetic latitudes from -60° to -90° and all MLT.

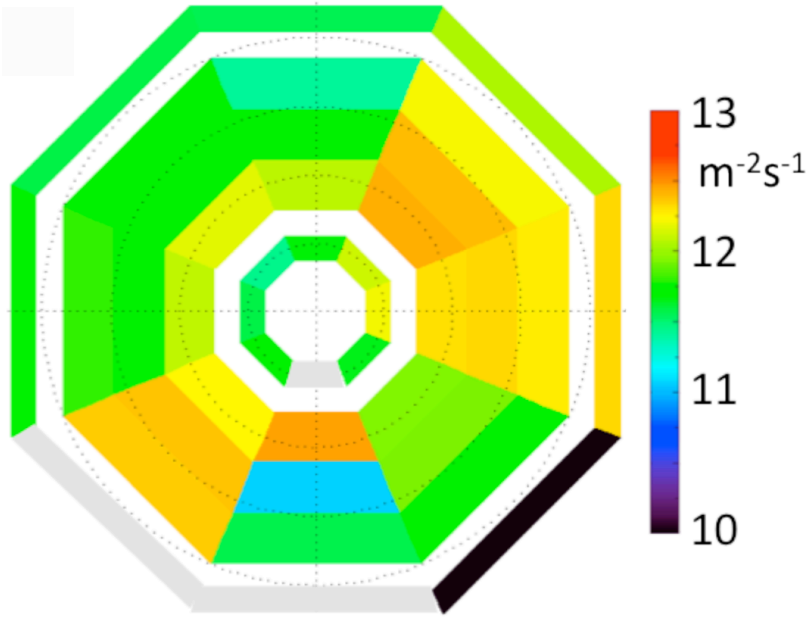

Figure 9: Modeled O^+ upwelling fluxes using the best-fit precipitation pattern and including neutral winds. The map is oriented with noon MLT on the top and dawn on the right. Cells colored grey indicate down welling fluxes.

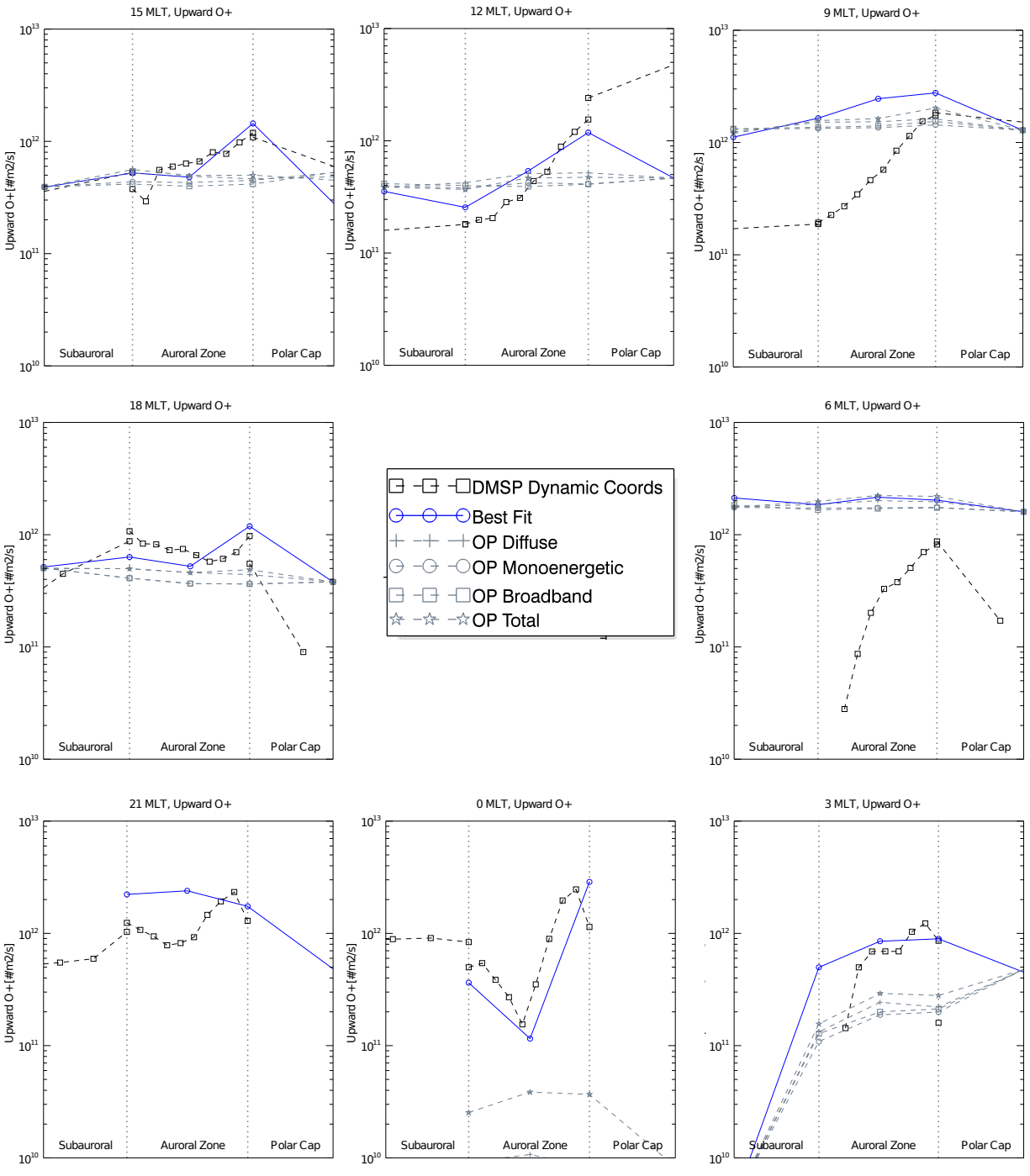

712

713 Figure 10: Comparison of observed (black squares) and modeled upwelling O^+ fluxes at
714 850 km in the southern hemisphere in DBRL coordinates using the best-fit (blue circles)
715 and OVATION Prime (grey lines and indicated symbols) precipitation patterns.
716 Downflowing model results indicated in Figure 5 are not shown. Noon MLT is on the top
717 and dawn is on the right. The format is the same as that in Figure 7.

718

719

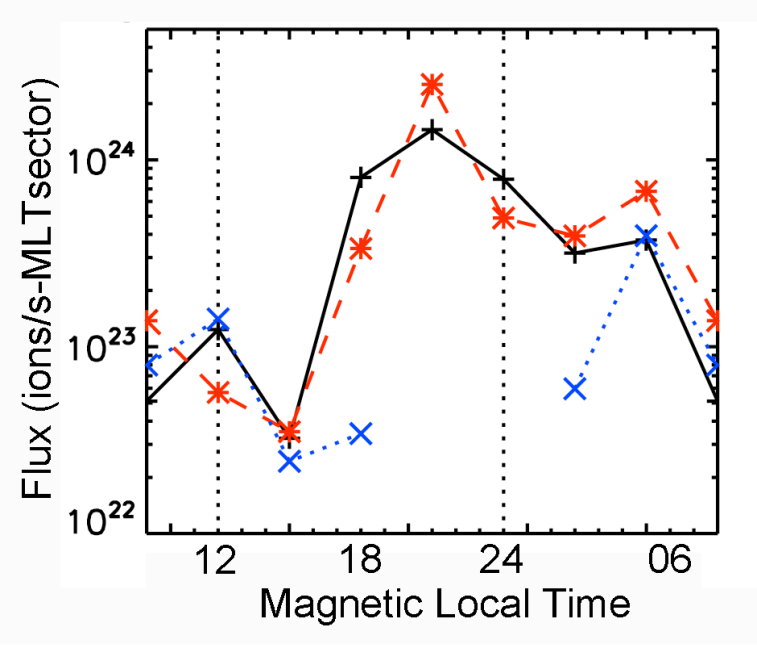

720

721 Figure 11. Observed (black pluses (+)) and modeled net upwelling fluxes in three-hour
722 magnetic local time bins. Red asterisks (*): model results from the best-fit electron
723 precipitation shown in Figure 8; blue crosses (×): model results with no electron
724 precipitation. The vertical dashed grey lines demark midnight and noon MLT.
725 Downflowing model results indicated in Figure 5 are not shown

726